Applied Physics A (2024) 130:667
https://doi.org/10.1007/s00339-024-07757-4

Applied Physics A
Materials Science & Processing

Luminescent and thermal Stability Properties of $SrBaMoO_4$:0.16Eu^{3+} Phosphor for solid-state lighting

Xuefeng Chen[1] · Shenlin Zhang[1] · Dejiang Dai[1] · Jun Lin[1]

Received: 13 May 2024 / Accepted: 12 July 2024 / Published online: 30 August 2024

Abstract
The red-emitting material $SrBaMoO_4$:0.16Eu^{3+} was synthesized by using a high-temperature solid-state method. X-ray diffraction (XRD) and fluorescence spectroscopy were employed to analyze the crystal structure and luminescent properties. The results revealed that the sintering temperature had an influence on the crystal structure of the samples, with an optimal sintering temperature of 800℃. $SrBaMoO_4$:0.16Eu^{3+} synthesized at 800℃ for 6.5 h exhibited a pure crystalline phase of $SrBaMoO_4$. The luminescent intensity of the $SrBaMoO_4$:0.16Eu^{3+} sample under excitation at 394 nm was tested at different temperatures. When the temperature reached 100℃, the luminescent intensity was 72.11% of the initial intensity, and the temperature reached 175℃, it dropped to 35.27% of the initial intensity. The sample demonstrated efficient excitation by blue light (464 nm), resulting the emission peak at 615 nm corresponding to the $^5D_0$-$^7F_2$ transition of Eu^{3+}. The luminescent intensity of the sample was found to increase with increasing Ba^{2+} concentration, reaching its maximum intensity when the Ba^{2+} doping concentration x was 0.27, followed by a gradual decreaseat excessive doping concentration, indicating concentration quenching. The CIE coordinates were calculated for the sample under excitation at 464 nm, revealing exhibited the best red emission at the Ba^{2+} doping concentration of $x = 0.27$. Additionally, first-principles calculations were used to determine the band structure and density of states of the sample.

Keywords Molybdate · Optical properties · Thermal stability · Eu^{3+}

1 Introduction

Light emission plays crucial role in human existence, serving as one of the essential conditions for our survival and development. It has emerged as a prominent field of study in this century, and advancements in illumination have revolutionized various areas of science and technology [1, 2]. To overcome these limitations, extensive research led to the design of Light-Emitting Diodes (LEDs), which offer advantages such as high efficiency, strong brightness, long lifespan, low energy consumption, and environmental friendliness. Solid state lighting (SSL) systems have proven to be extremely dependable as well. In recent times, SSL systems have effectively replaced consumption incandescent lamps [3]. The investigation into lighting systems has resulted in the discovery of phosphors, which are solid substances primarily composed of hosts and dopants. Rare earth (RE) or small amounts of transition metal ions are typically typically as dopants [4]. Phosphors have been identified a fundamental requirement for the generation of SSL [5–9].

Molybdate-based phosphors demonstrate exceptional luminescent performance and stability, offering the added benefit of facile synthesis at low temperatures. In double molybdate phosphors, MoO_4^{2-} adopts a tetrahedral structure, characterized by Mo^{6+} positioned at the center and surrounded by four O^{2-} ionsions at the vertices [10]. After doping Eu^{3+} into molybdate-based phosphors, it assumes an asymmetrical position, leading to phosphors with enhanced color rendering and outstanding luminescent properties. Thus, they are widely regarded as optimal luminescent materials.

✉ Xuefeng Chen
285891069@qq.com

[1] Guizhou Highway Engineering Group Co., Ltd, Guiyang, China

2 Experiment

2.1 Sample preparation

In this experiment, $SrBaMoO_4$:0.16Eu^{3+} red phosphors were synthesized using the high-temperature solid-state method. $SrCO_3$ (A.R.), $BaCO_3$ (A.R.), MoO_3 (A.R.), and Eu_2O_3 (A.R.) were weighed according to a specific stoichiometric ratio. The raw materials were mixed and placed in a milling jar, and a suitable amount of anhydrous ethanol was added according to the total sample mass. The milling jar was then the ball mill and milled for 10 h. Subsequently, the milling jar and the alumina balls were rinsed with anhydrous ethanol, and the sample was dried in an 800℃ constant temperature drying oven for 4 h. The dried powder was finely ground using an agate mortar and then placed in an alumina crucible. The sample was then sintered at different temperatures (600 ℃, 700 ℃, 800 ℃, 900 ℃, 1000 ℃) for 6.5 h to obtain the desired samples. The optimal sintering temperature was determined to be 800 ℃.

2.2 Characterization methods

The crystal structure of the samples was tested using a Rigaku SmartLab X-ray diffractometer (XRD) from Japan. The anode metal used was Cu, with a working voltage and current of 40 kV and 40 mA, respectively. The scanning range was (10–80)°. The excitation and emission spectra of the samples were analyzed using a HORIBA Fluoromax-4 spectrofluorometer. All tests were conducted at room temperature.

3 Results and Discussion

3.1 Crystal structure and XRD Analysis of the Phosphors

Figure 1 shows the crystal structure of $SrBaMoO_4$:0.16Eu^{3+} is represented.Fig. 2 shows the XRD spectra obtained under the same sintering time of 6 h and the same doping concentration at different sintering temperatures. From Fig. 1, it can be observed that the main diffraction peaks match well with the JCPDS No. 08–0482 standard card, with lattice constants a = b = 5.3887 Å, c = 11.9759 Å, α = β = γ = 90°, and space group I41/a (88) [11]. This indicates the formation of SrBaMoO4 phase, which belongs to the tetragonal scheelite-type structure. The main peak position of SrBaMoO4 relatively stable at different sintering temperatures,suggesting minimal change in the crystal structure with varying calcination

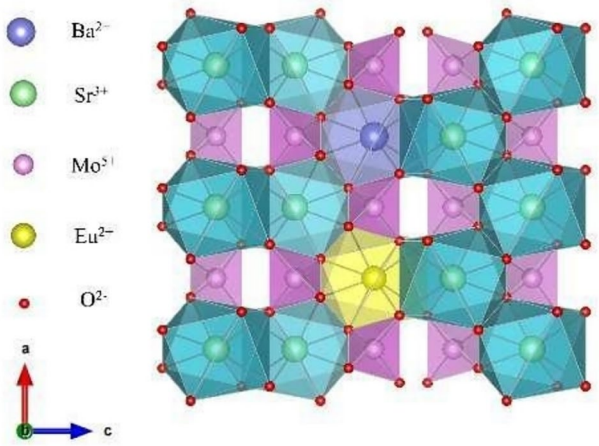

Fig. 1 Structure of SrBaMoO4:0.16Eu3 + crystal

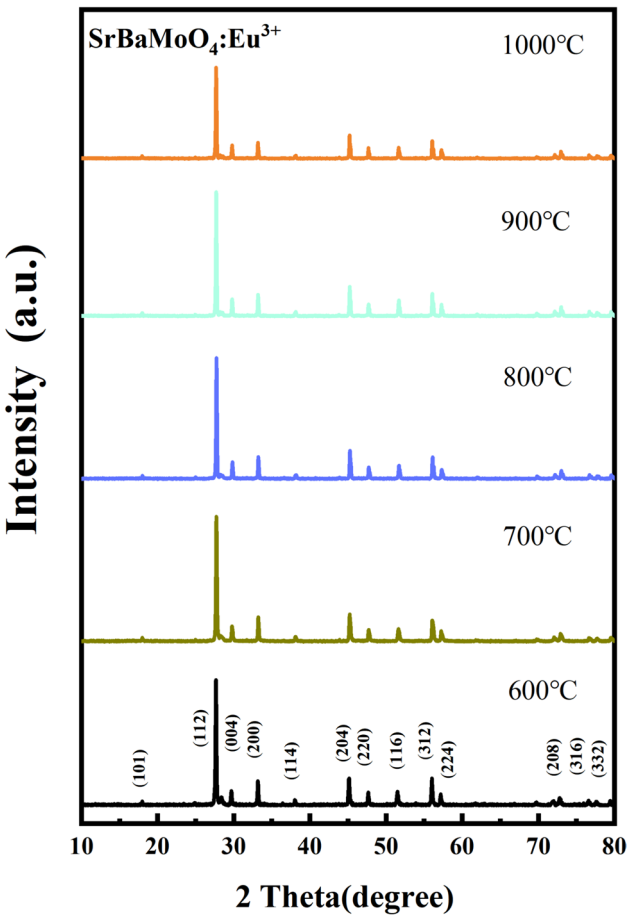

Fig. 2 XRD spectra of SrBaMoO4:0.16Eu3 + sintered at 600℃, 700℃, 800℃, 900℃, and 1000℃ respectively

temperature. From Fig. 1 and Table 1, it can be seen that at a sintering temperature of 600℃, there are some impurity peaks, and the main peak at around 27.7° aligns with the

Table 1 XRD data of the samples at different sintering temperatures

Sample	2θ	Diffraction peak intensity	FWHM
600 ℃ 6h	27.7	2753	0.121
700 ℃ 6h	27.7	3413	0.16
800 ℃ 6h	27.7	4043	0.112
900 ℃ 6h	27.7	3807	0.114
1000 ℃ 6h	27.7	3378	0.118

main peak of the material obtained under high-temperature conditions, albeit with weak intensity. The indicats poor crystallinity and incomplete reaction under the sintering condition of 600℃. As the sintering temperature increases, the intensity of the diffraction peaks becomes more pronounced, indicating an enhanced crystallinity of the material. At a sintering temperature of 800℃, the diffraction peaks reaches their maximum intensity, and the full width at half maximum (FWHM) of the peaks is minimized. However, further increase in temperature to 1000℃ leads to a decrease in the intensity of the diffraction peaks, indicating poorer crystalline phase compared to that obtained under the sintering condition of 800℃

The Fig. 3 illustrates the XRD analysis of $SrBaMoO_4$:0.16Eu^{3+}. Upon observing the XRD pattern of the sample, it is evident that it closely matches the characteristic peaks of the standard JCPDS card No. 08–0482 for $SrBaMoO_4$, This indicates the absence of any other impurity phases. Formation, it suggests the formation of the tetragonal scheelite structure phase of $SrBaMoO_4$, and the small amount of Ba^{2+} and Eu^{3+} doping has not impact on the crystal structure of the material. It belongs to the I41/a (88) space group [12]. The lattice constants of the sample are calculated and listed in Table 2. From the table, it is observed that the lattice parameters gradually decrease with the increase of Ba^{2+} concentration. The grain size was calculated using the Scherrer equation, $D = K\lambda/\beta COS\theta$, where K is the Scherrer constant (0.89), λ is the wavelength of Cu Kα radiation (0.1540 nm), β is the full width at half maximum, θ is the diffraction angle, and D represents the grain size. According to calculations, the grain size is 5.3 μm.

Figure 4 shows the SEM images of $SrBaMoO_4$:0.16Eu^{3+} samples sintered at different temperatures: 600℃, 800℃, 900℃, and 1000℃. It is clear from the images that the average grain size of the samples increases with higher sintering temperatures. The average grain size of the sample sintered at 800℃ is approximately 3.85 μm, while it increases to about 5.3 μm at a temperature of 1000℃. Temperature plays a significant role in the solid-state reaction, impacting the reaction and expansion capabilities of the material, thus resulting in continuous grain growth (Table 3).

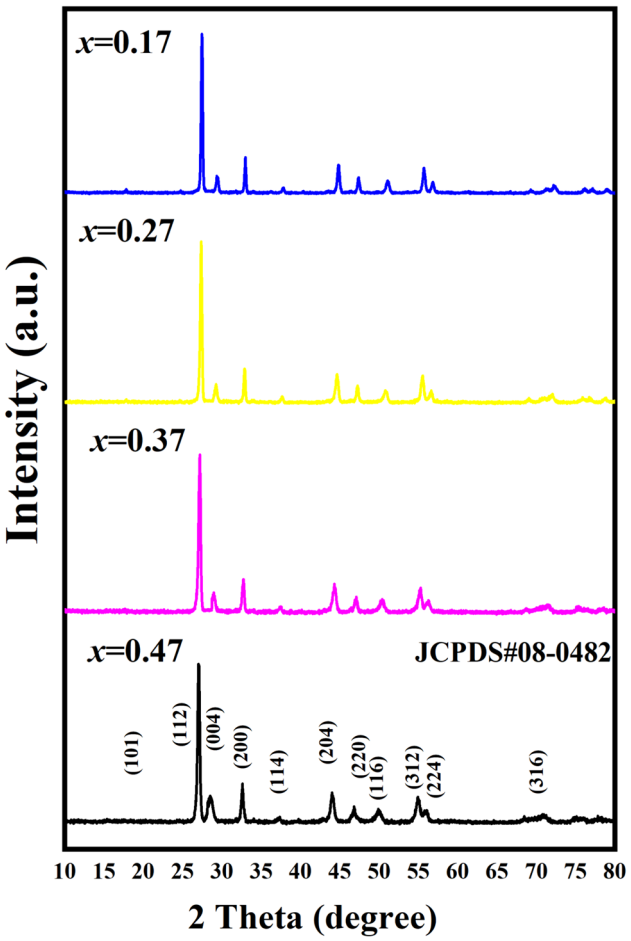

Fig. 3 XRD spectra of SrBaMoO4:0.16Eu3 +

3.2 Optical Properties of $SrBaMoO_4$:0.16Eu^{3+}

Figure 5 displays the excitation spectrum of $SrBaMoO_4$:0.16Eu^{3+} at a monitoring wavelength of 615 nm. Within the wavelength range of 350–550 nm, all samples exhibit narrow absorption peaks attributed to the 4*f*-4*f* transitions of Eu^{3+}. Specifically, two prominent peaks are observed at 394 nm ($^7F_0$-$^5L_6$) and 464 nm ($^7F_0$-$^5D_2$) [13–15]. Although the positions of the excitation peaks remain mostly consistent at different temperatures, the intensity of the emission varies. The emission spectra

Table 2 Cell parameters of the samples $SrBaMoO_4$:0.16Eu^{3+}

Sample	Cell parameters			
	a(Å)	*b*(Å)	*c*(Å)	v(Å)
$Sr_{0.71}Ba_{0.17}MoO_4$:0.16Eu^{3+}	5.8203	5.8203	12.2012	413.32
$Sr_{0.62}Ba_{0.27}MoO_4$:0.16Eu^{3+}	5.4027	5.4027	12.1758	355.4
$Sr_{0.69}Ba_{0.37}MoO_4$:0.16Eu^{3+}	5.4863	5.4863	11.8073	355.39
$Sr_{0.45}Ba_{0.47}MoO_4$:0.16Eu^{3+}	5.9235	5.9235	9.6663	339.17

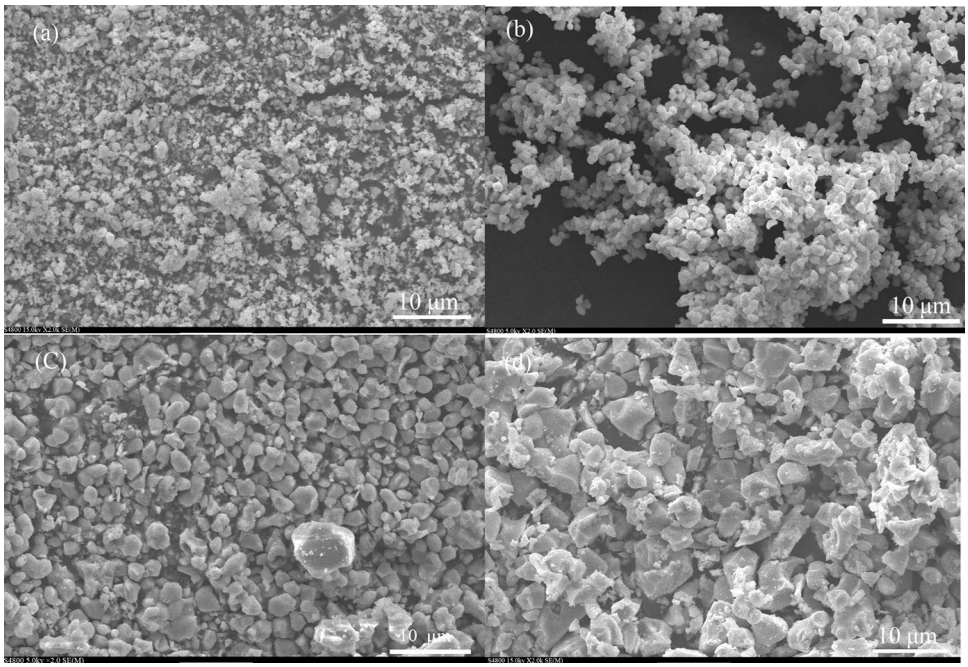

Fig. 4 The SEM of SrBaMoO4: 0.16Eu3 + sintered at **a** 600℃, **b** 800℃, **c**900℃, and **d** 1000℃

Table 3 The CIE color coordinates of $SrBaMoO_4$:0.16Eu^{3+}under excitation at 464 nm

Excitation wavelength of the sample (nm)		CIE Coordinates	
		x	y
$Sr_{0.71}Ba_{0.17}MoO_4$:0.16Eu^{3+}	464	0.633	0.3585
$Sr_{0.62}Ba_{0.27}MoO_4$:0.16Eu^{3+}	464	0.6434	0.3521
$Sr_{0.53}Ba_{0.37}MoO_4$:0.16Eu^{3+}	464	0.6174	0.3687
$Sr_{0.45}Ba_{0.47}MoO_4$:0.16Eu^{3+}	464	0.5974	0.3819
$Sr_{0.85}MoO_4$:0.16Eu^{3+}	464	0.6305	0.3602

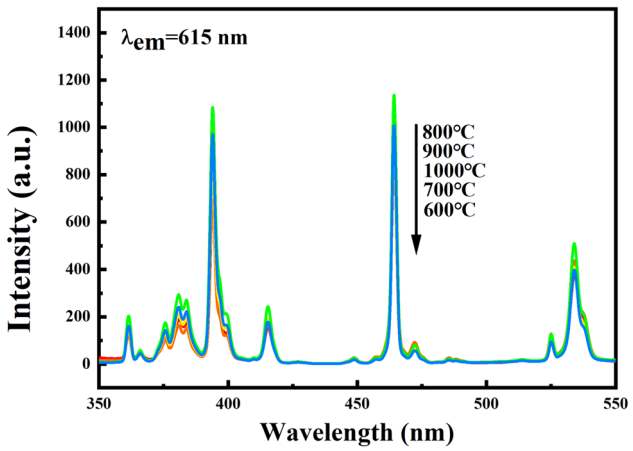

Fig. 5 Excitation spectra of SrBaMoO4:0.16Eu3 + at different sintering temperatures

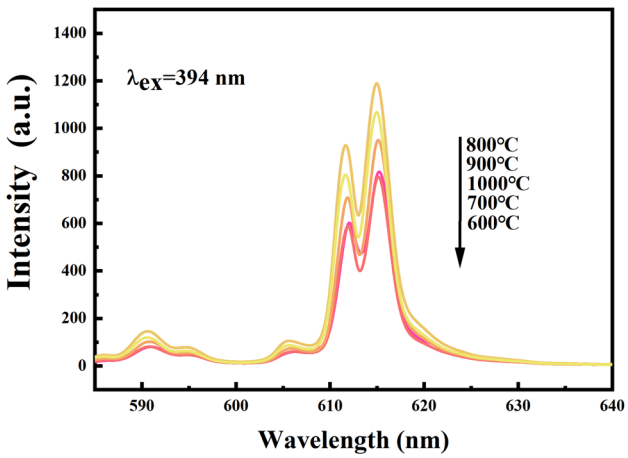

Fig. 6 Emission spectra(394 nm) of SrBaMoO4:0.16Eu3 + at different sintering temperatures

of $SrBaMoO_4$:0.16Eu^{3+} under excitation at 394 nm and 464 nm are present in Fig. 6 and 7, respectively. From Fig. 6, it is evident that the emission peaks from 585 to 660 nm consist of several sharp peaks, with the primary emission peak located at 615 nm, which is the characteristic emission peak of Eu^{3+}. As the sintering temperature, the emission intensity enhances, reaching its maximum at 800 ℃. However, when the sintering temperature surpasses 1000℃, the emission performance of the sample deteriorates. Solid-state reactions are influenced by various factors. Firstly, the temperature affects the contact area, surface area between solid phases, and the structural differences between the product and reactant phases.

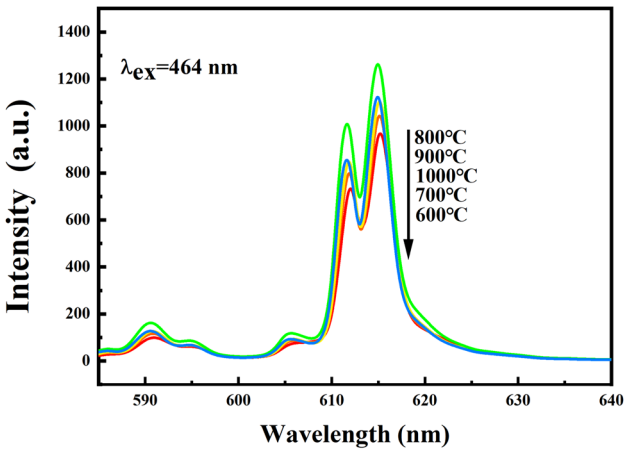

Fig. 7 Emission spectra(464 nm) of SrBaMoO4:0.16Eu3 + at different sintering temperatures

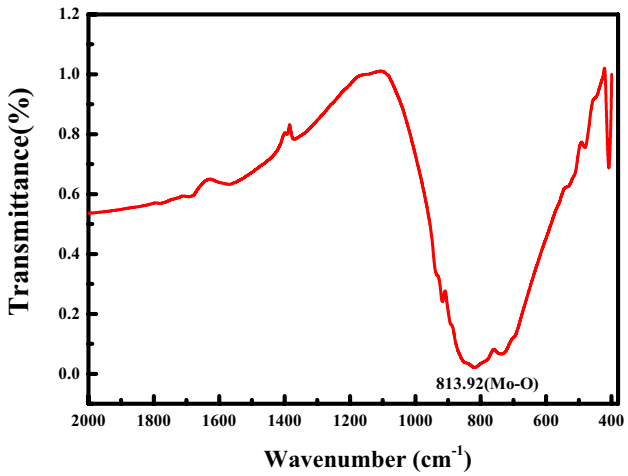

Fig. 8 FT-IR spectrum of SrBaMoO4:0.16Eu3 +

Additionally, temperature, crystal structure, and defects affect the diffusion rate of ions through different phases, particularly the product phase. Hence, sintering temperature plays a vital role in determining the rate of solid-state reactions. From XRD Fig. 2, it can be seen that the crystallinity of the sample sintered at 800℃ is higher than that sintered at 1000 ℃. Furthermore, SEM Fig. 4 also reveals that the average grain size of the sample sintered at 800 ℃ is smaller compared to that sintered at 1000 ℃. Generally, there is a positive relationship between solid-state reaction and temperature; a higher temperature enhances the reaction force and expansion force of the material, resulting in larger thermal motion of particles and a significantly increased self-diffusion coefficient, thus accelerating sintering. In conclusion, the optimal sintering temperature for $SrBaMoO_4$:0.16Eu^{3+} material is 800 ℃.

Infrared spectroscopy, specifically Fourier-transform infrared spectroscopy (FT-IR), is a crucial method for characterizing samples and providing insight into their structural properties. Figure 8 shows the infrared spectrum of the sample $SrBaMoO_4$:0.16Eu^{3+} obtained after sintering at 800 °C for 6.5 h, as shown in Fig. 8. There are two strong absorption bands observed: the strong absorption peak at approximately 813.92 cm^{-1} is characteristic of the MoO_4^{2-} group in the infrared spectrum. The MoO_4^{2-} group consists of molybdenum ions surrounded by four coordinated oxygen ions, exhibiting a tetrahedral Mo–O symmetry with the υ3 anti-symmetric stretching vibration at 414 cm^{-1}, Furthermore, there is a weaker absorption peak observed at 1614 cm^{-1}, which corresponds to the bending vibration of H–O–H, which is a characteristic vibration of water. These observations indicate that the sample possesses the complete crystal phase structure of $SrBaMoO_4$:0.16Eu^{3+}.

3.3 The optical properties of $SrBaMoO_4$:0.16Eu^{3+}

The excitation spectrum of $SrBaMoO_4$:0.16Eu^{3+} monitored at 615 nm is displayed in Fig. 9 The graph clearly indicates that the wide excitation band ranging from 250 to 330 nm, observed in the excitation spectrum, belongs to the ultraviolet region. This band is primarily composed of O^{2-}-Mo^{6+} charge transfer (CTB) and O^{2-}-Eu^{3+} charge transfer (CTB). The sharp excitation lines in the range of 330 nm to 550 nm belong to the near-ultraviolet to visible light region and can be attributed to the characteristic spectral lines of the activator Eu^{3+} in the 4*f*-4*f* transition. Among these sharp excitation lines, the most prominent ones are at 394 nm, 464 nm, and 535 nm, corresponding to the transitions $^7F_0 \rightarrow {}^5L_6$, $^7F_0 \rightarrow {}^5D_2$, and $^7F_0 \rightarrow {}^5D_1$ [16]. Furthermore, when the Ba^{2+} doping concentration is equal to 0.27, the intensity of the excitation peaks reaches its maximum value. This indicates

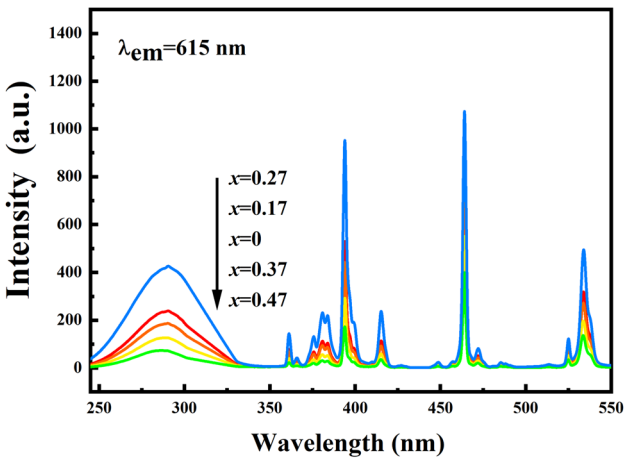

Fig. 9 The excitation spectrum of SrBaMoO4:0.16Eu3 + monitored at 615 nm

that $SrBaMoO_4$:0.16Eu^{3+} can be effectively excited by 464 nm visible light.

As shown in Fig. 10, the emission spectra of $SrBaMoO_4$:0.16Eu^{3+} under excitation at 394 nm and 464 nm are presented. From the graph, the emission spectra obtained from exciting the $SrBaMoO_4$:0.16Eu^{3+} samples at 464 nm wavelengths exhibit identical characteristics and positions. The emission spectra of $SrBaMoO_4$:0.16Eu^{3+} consist of a series of Eu^{3+} emission peaks, which are characteristic peaks of Eu^{3+}. The peaks observed at 611 nm and 615 nm correspond to the $^5D_0 \rightarrow {}^7F_J$ (J = 0, 1, 2, 3, 4) transitions of Eu^{3+}. Specifically, the transition at 611 nm corresponds to the magnetic dipole transition of $^5D_0 \rightarrow {}^7F_1$, and $^5D_0 \rightarrow {}^7F_2$ for electric dipole transition (615 nm). From Fig. 10 it can be observed that the emission peak at 615 nm is the dominant peak, indicating the forced electric dipole transition $^5D_0 \rightarrow {}^7F_2$ in Eu^{3+}, suggesting the presence of Eu^{3+} occupying an asymmetric center position. With an increase in the Ba^{2+} content, the relative luminescence intensity of the samples reaches its maximum at 615 nm, and when the Ba^{2+} doping concentration is 27 mol%, The lattice type remains unchanged. The lattice type remains unchanged. However, when the Ba^{2+} doping concentration exceeds 27 mol%, the luminescence intensity of the material decreases. This decease may be attributed to the inherent matrix characteristics of molybdate, leading to concentration quenching.

3.4 Thermal analysis of $SrBaMoO_4$:0.16Eu^{3+}

Thermal luminescent analysis was conducted on fluorescent powder to gain insights into its impact on light radiation and color rendering index. In this study, the temperature characteristics of $SrBaMoO_4$:0.16Eu^{3+} were analyzed, specifically examining its thermal stability. The sample was excited at

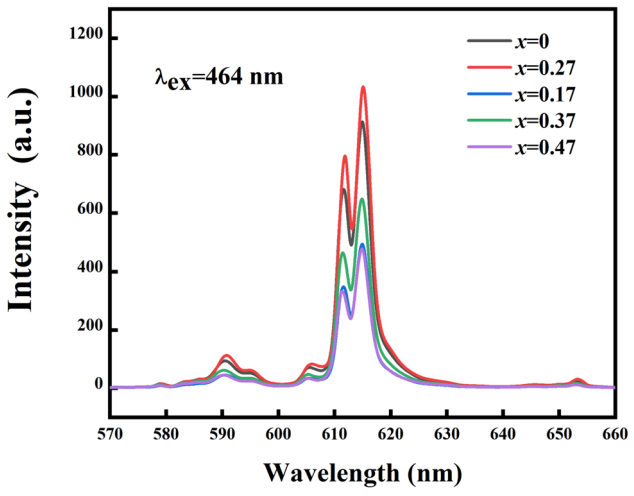

Fig.10 The comparison of the emission spectra of SrBaMoO4:0.16Eu3 + under excitation at 464 nm

394 nm, and the luminescent intensity at 615 nm was measured at temperatures of 30 °C, 50 °C, 75 °C, 100 °C, 125 °C, 150 °C, 175 °C, 200 °C, 225 °C, 250 °C, and 275 °C. The variation in luminescent intensity with temperature is shown in Fig. 11(a). From the graph, it can be observed that the characteristic emission peaks corresponding to the $^5D_0 \rightarrow {}^7F_1$ and $^5D_0 \rightarrow {}^7F_2$ transitions of Eu^{3+} ions can be seen at different temperatures [17], the $^5D_0 \rightarrow {}^7F_2$ transition exhibits the highest intensity among the observed transitions. However, as the temperature rises, the luminescent intensity of the sample progressively diminishes. the temperature dependence is shown in the insert of Fig. 11(a). Accompany with the temperature rises from 30 °C to 125 °C, the luminescent intensity decreases rapidly, indicating temperature quenching. However, no change in the emission spectral peak position is observed. This phenomenon is attributed to the increase in lattice thermal vibrations with temperature, resulting in an increased probability of non-radiative transitions and a decrease in the luminescent intensity [18, 19]. However, the rate of non-radiative electron transitions is also dependent on temperature to some extent. For the $SrBaMoO_4$:0.16Eu^{3+} sample, when the temperature reaches 100 °C, the luminescent intensity is approximately 72.11% of the initial intensity. At a temperature of 175 °C, the luminescent intensity decreases to approximately 35.27% of the initial intensity. The temperature at which the luminescent intensity decreases to around 50% of the initial intensity is defined as the thermal quenching temperature, denoted as T 0.5. For $SrBaMoO_4$:0.16Eu^{3+}, T is approximately 422 K.

The thermal quenching activation energy (ΔE) can be determined using the Struck and Fonger model, which calculates the relationship between the luminescent intensity (I(T)) and the initial intensity (I_0).

$$\frac{I(T)}{I_0} = \left[1 + \frac{S}{A}\exp\left(-\frac{\Delta E}{K_B T}\right)\right]^{-1} \quad (1)$$

According to Eq. 1, where A is the radiative decay rate of Eu^{3+}, S is the thermal quenching rate, By incorporating the Boltzmann constant (KB), a constant S/A, and the activation energy of thermal quenching (ΔE), we can transform it into Eq. 3.3. By calculating the results, we obtain the plot of In[I_0/I(T)—1] against I/(KBT) as shown in Fig. 11(b), which leads to the determination of the activation energy of thermal quenching (ΔE) as 0.302 eV.

$$\frac{I_0}{I(T)} - = 1\frac{S}{A}\exp\left(\frac{\Delta E}{K_B T}\right)$$

$$In\left[\frac{I_0}{I(T)}\right] - = In\frac{5}{A} - \frac{\Delta E}{K_B T} \quad (2)$$

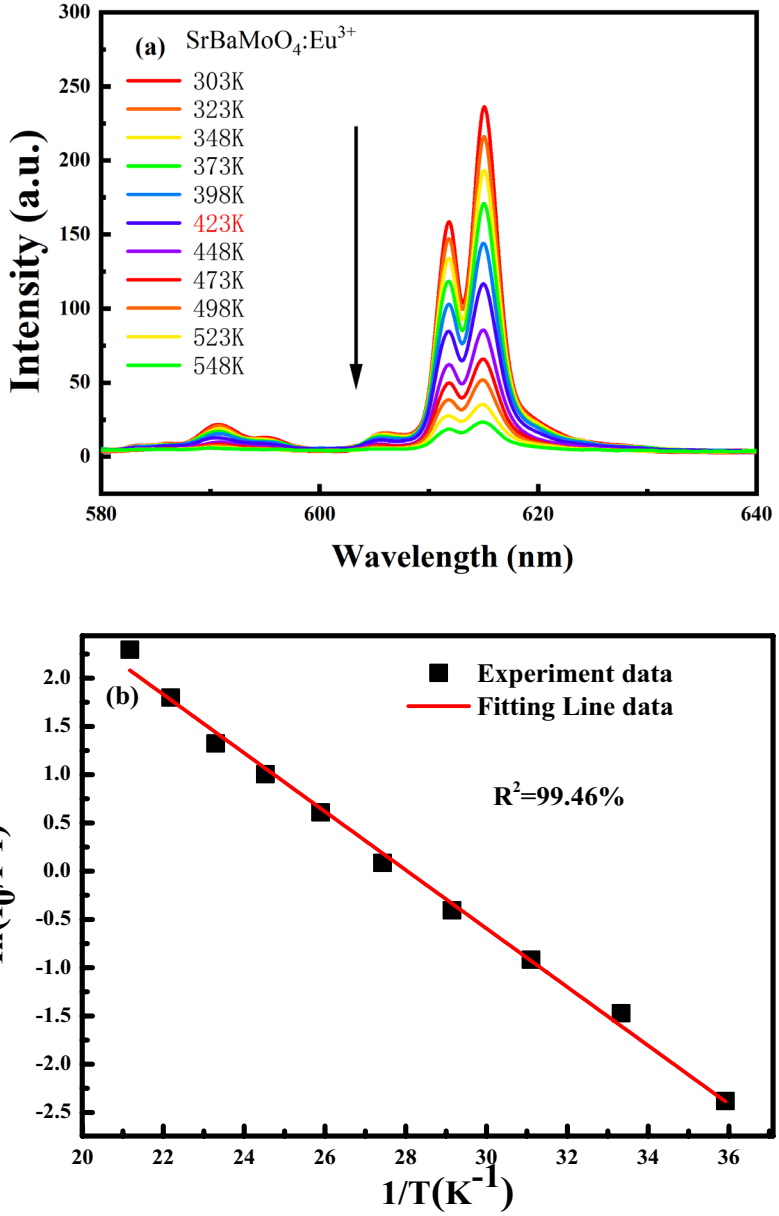

Fig. 11 **a** The emission spectra of SrBaMoO4:0.16Eu3 + at 394 nm excitation wavelength and different temperatures. The inset represents the relative luminescence intensity at the corresponding temperature at 394 nm. **b**. A plot showing the relationship between In[I0/I(T)-1] and I/(KBT)

3.5 Colorimetric analysis of the sample

From Fig. 12, it is evident that the calculated color coordinates of the sample, the calculated color coordinates of the sample $SrBaMoO_4$:0.16Eu^{3+} (x = 0.6434, y = 0.3521) are closer to the National Television System Committee (NTSC) standard (x = 0.670, y = 0.330) compared to the sample $SrBaMoO_4$:0.16Eu^{3+} without Ba^{2+} doping (x = 0.6305, y = 0.3602) [20]. Figure 12 also demonstrates that as the Ba^{2+} doping concentration increases, the color coordinates shift towards the red region, and when the doping amount reaches 47 mol%, the color coordinates shift back. The sample with a Ba^{2+} doping concentration of 27 mol% exhibits the highest relative luminescence intensity.

4 Theoretical calculation results and analysis

Figure 13 illustrates the calculated band structure, and Table 4 presents the corresponding band gap values. The band gap of $SrMoO_4$ is determined to be 3.6817 eV, which is in close agreement with the previously reported calculated value of 3.59 eV. From Table 4, it can be observed that the

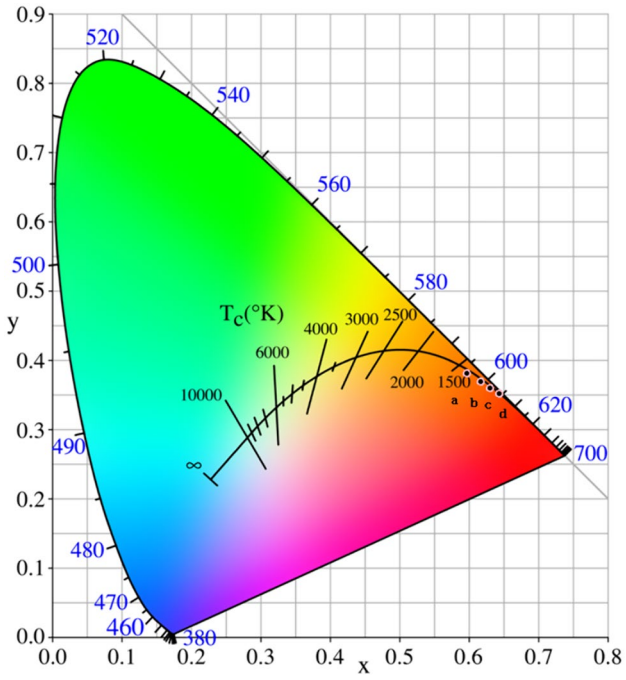

Fig. 12 The color coordinate chart of the samples (where a represents x = 0.47, b represents x = 0.37, c represents x = 0.17, and d represents x = 0.27)

doping of Eu^{3+} in $SrMoO_4$ increases the band gap value from 3.6817 eV to 3.7131 eV. However, the co-doping of Ba^{2+} and Eu^{3+} in $SrBaMoO_4$ reduces the band gap value from 3.7131 eV to 3.6804 eV. This decrease can be attributed to the presence of numerous oxygen defects and surface metallic clusters caused by Ba^{2+} doping. As the grain size of the sample increases, the crystal band gap decreases. With the reduction in the host band gap, with the increased participation of electrons in the emission process of Eu^{3+}, there is an overall enhancement in the emission spectral intensity. Additionally, as the crystal band gap decreases, electrons in the valence band are more easily excited to the ground state, thereby contributing to the excitation process of Eu^{3+} and further enhancing the emission spectral intensity.

To further investigate the luminescence mechanism of the samples, the total and partial density of states (DOS) of the studied phosphors are presented in Fig. 14. The figure clearly depicts a significant overlap between the O-p and V-d states indicates the covalent nature of the bond. The conduction band is mainly composed of Mo-d states and Sr-f states from the Fermi level, along with some contributions from O-p states. The total and partial DOS after Eu^{3+} doping are shown in Fig. 14. In the case of Eu-doped $SrBaMoO_4$, the valence band is primarily dominated by O-p, Mo-d, Eu-p,

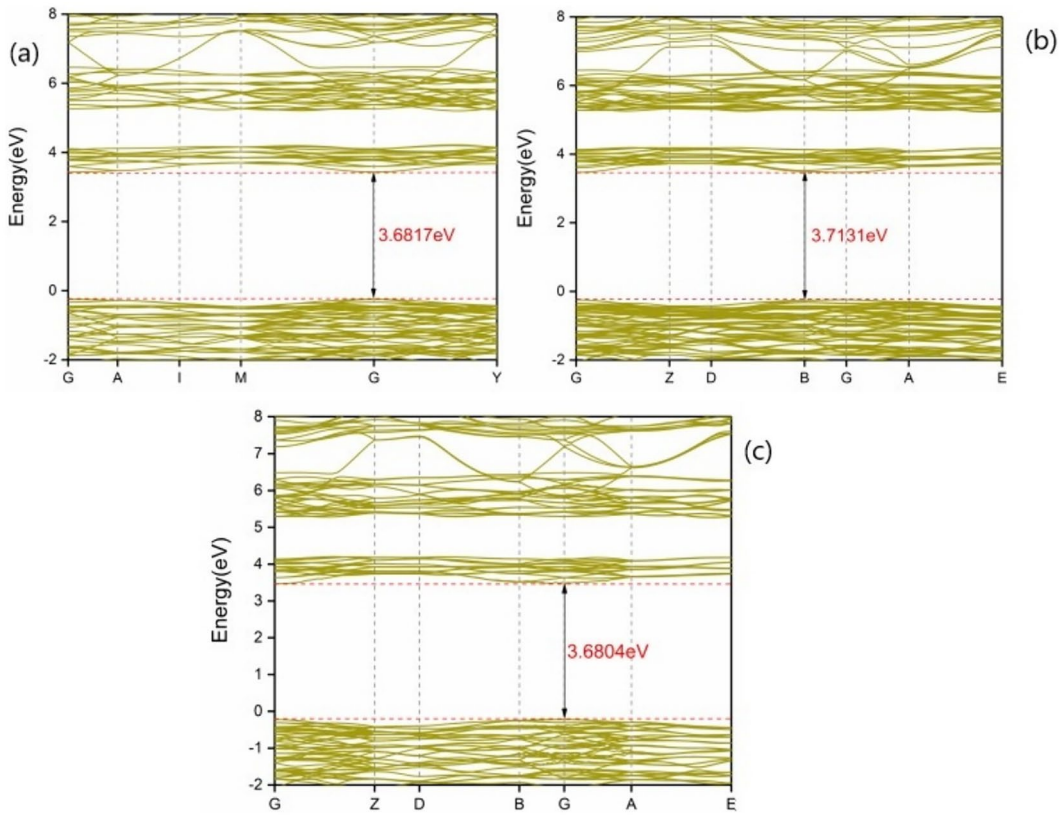

Fig. 13 **a** Calculated band structure of SrMoO4, **b** Calculated band structure of SrMoO4: Eu3 + , and **c** Calculated band structure of SrBaMoO4: Eu3 +

Table 4 Band gap values of SrMoO4, SrMoO4: Eu^{3+}, and SrBaMoO4: Eu^{3+}

Material	Band gap(eV)
SrMoO4	3.68
SrMoO4:Eu^{3+}	3.71
SrBaMoO4:Eu^{3+}	3.68

and Eu-d states, while the conduction band is mainly contributed by Mo-d and Sr-f states, with some additional contributions from O-p, Eu-p, and Eu-d states. From Fig. 14, it can be observed that the replacement of Ba^{2+} in the system leads to enhanced overlapping between the Mo-d and O-p orbitals near the Fermi level (− 5 to 0 eV), strengthening the covalent bond. Consequently, this heightened probability of electron transition intensifies the absorption of UV light.

5 Conclusion

Fabrication of $SrBaMoO_4$:0.16Eu^{3+} phosphors was performed using a high-temperature solid-phase method. The optimal conditions for preparation were investigated. Different concentrations of Ba^{2+} ions were used in the synthesis of $SrBaMoO_4$:0.16Eu^{3+} phosphors. According to CIE calculations, as the Ba^{2+} doping concentration increased, the color coordinates shifted towards the red region. However, when the doping amount reached 47 mol%, the color coordinates shifted back. The sample with a Ba^{2+} doping concentration of 27 mol% exhibited the highest relative luminescence intensity. The temperature characterisation of $SrBaMoO_4$:0.16Eu^{3+}reveals that the thermal quenching temperature of the samples, $T_{0.5}$ = 422 K, and the activation energy of the thermal quenching, ΔE = 0.302 eV. VASP calculations revealed that Ba^{2+} doping resulted in a reduction of

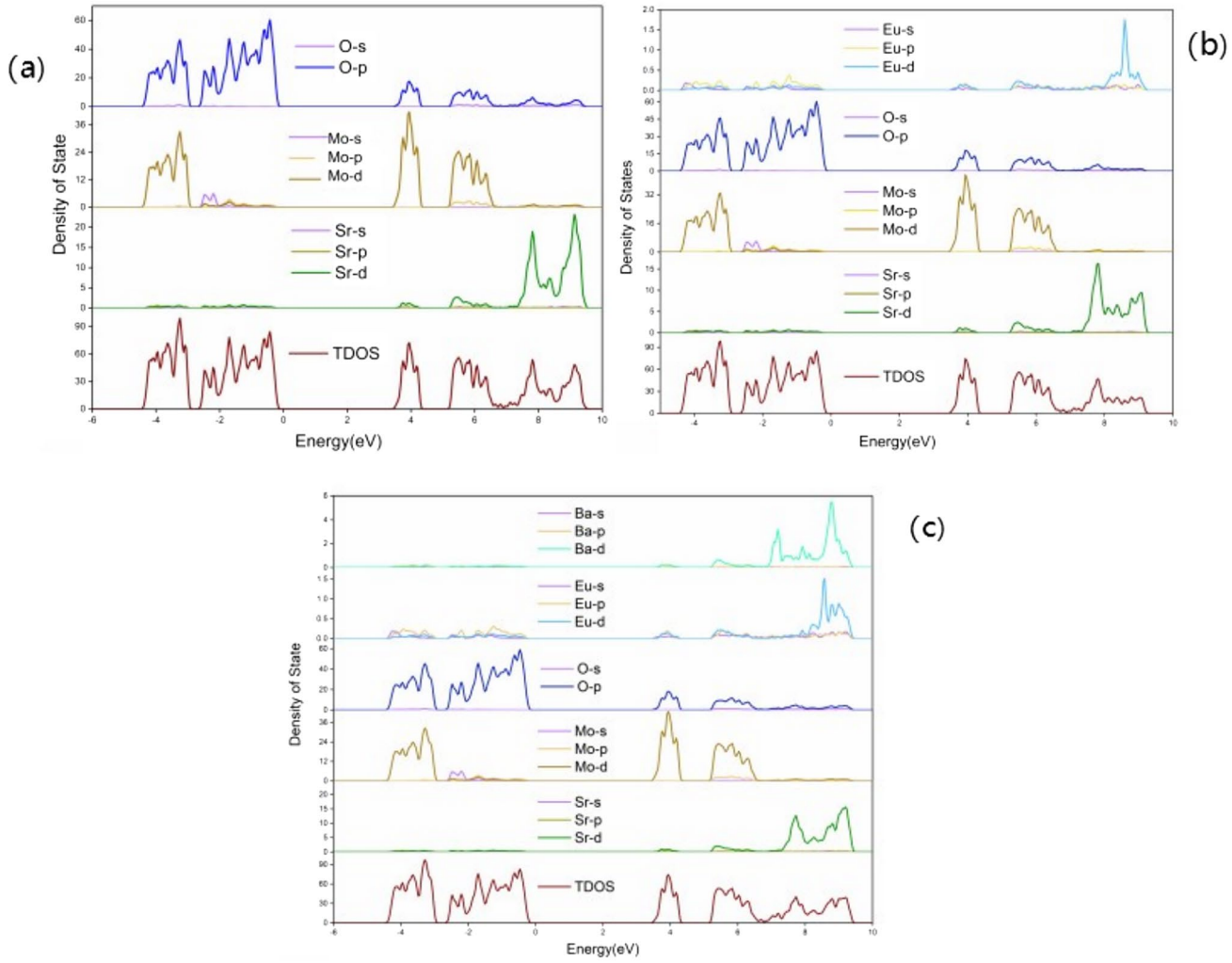

Fig. 14 **a** Calculated total density of states (DOS) and partial density of states (PDOS) for SrMoO4, **b** Calculated total DOS and PDOS for SrMoO4: Eu3 +, and **c** Calculated total DOS and PDOS for SrBaMoO4: Eu3 +

the band gap of $SrBaMoO_4$:0.16Eu^{3+}, leading to a redshift in the charge transfer absorption band of $[MoO_4]^{2-}$. Moreover, Ba^{2+} doping decreased the host band gap. The high-temperature solid-phase method allowed for increased participation of electrons in the luminescent center of Eu^{3+} ions, resulting in enhanced energy transfer efficiency. Density of states calculations confirmed that Ba^{2+} doping enhanced the covalence of the Mo–O bond, thereby increasing the likelihood of electron transitions.

Author contributions Chen Xuefeng: contributed to the conception of the study and performed, the experiment contributed significantly to analysis and manuscript preparation; Zhang Shenlin: performed the data analyses and wrote the manuscript and helped perform the analysis with constructive discussions; Dejiang Dai:Conducted experimental operations and data collection, participated in drafting the initial manuscript. Jun Lin:In charge of laboratory data collection and creating charts.

Data availability The data that support the findings of this study are available on request from the corresponding author. The data are not publicly available due to privacy or ethical restrictions.

References

1. Y Zhang, Prepartion and Properties of $KLa(MoO)_2$:Yb, Ho, Tm white phosphor, Chinese Journal of Luminescence. 34(2017).
2. X. Ju, X. Li, W. Li, W. Yang, C. Tao, Luminescence properties of $ZnMoO_4$:Tb^{3+} green phosphor prepared via co-precipitation. Mater. Lett. **68**, 17 (2011)
3. D.D. Yengkhom, G.S. Ningombam, T.D. Singh, Luminescence enhancement and tunable color emission in Eu/Dy/Sm codoped CaW(1–x)MoxO4 phosphor. Inorg. Chem. Commun. (2022). https://doi.org/10.1016/j.inoche.2022.109571
4. P.Y. XiaofangYu, Wanda Kang;Ruyan Song;Yongqing Zheng;Xiaoyun Mi., Color-tunable luminescence and energy transfer properties of Ca15Sr15(PO4)2:Dy3+, Tb3+ phosphor via hydrothermal synthesis. J. Lumin. (2022). https://doi.org/10.1016/j.inoche.2022.109571
5. L. He, X. Wei et al., Synthesis and photoluminescence of a full-color emitting phosphor $Gd_2MoB_2O_9$:$Eu^{3+}Tb^{3+}$ for white light LEDs. J. Funct. Materials. (2014). https://doi.org/10.1016/j.dyepig.2018.09.012
6. Debarati Das, Santosh Kumar Gupta, A. P. Srivastava, P Utpalla, Kathi Sudarshan. (2020). Probing emission and defects in $BaW_{1-x}Mo_xO_4$ solid solutions: Achieving color tunable luminescence by W/Mo ratio and size manipulation. New Journal of Chemistry.
7. K. Gzhan, X. Xiuzhen, Y. Jun, M. Dongsen, L. Guanzhong, Color-tunable luminescence properties of Sm^{3+}/Dy^{3+} co-doped $NaLa(MoO_4)_2$ phosphors and their energy. J. Mater. Sci. (2017). https://doi.org/10.1007/s10853-017-0863-6
8. S.W. Park, B.K. Moon et al., Crystal structure, electronic structure, and photoluminescent properties of SrBaMoO4:Tb^{3+} phosphors. Mater. Res. Bull. (2015). https://doi.org/10.1016/j.materresbull.2015.04.066
9. Wang, J (Wang, Jing); Song, MJ (Song, Mingjun); Seo, HJ (Seo, Hyo Jin).Luminescence and energy transfer in $BaY_2(MoO_4)_4$:Tb^{3+},Eu^{3+} phosphors and bifunctional applications in thermometry and light emitting diodes , Journal of Luminescence. 222(2022) .
10. M Yu, X Xu, W Zhang, X Chen, Y Huang. Luminescence properties of $Ca_{2.85}Li_{0.15}(PO_4)_{1.85}(SO_4)_{0.15}$: Dy^{3+} .Journal of Alloys and Compounds. 10(2019).
11. L. Li, W. Zi, G. Li, L. Shi, G. Ji, S. Gan, H. Zou, X. Xu, Hydrothermal synthesis and luminescent properties of $NaLa(MoO_4)_2$:Dy^{3+} phosphors. J. Solid State Chem. (2012). https://doi.org/10.1016/j.jssc.2012.03.003
12. Y. Hui, X. Shi, L. Huang, X. Kang, D. Pan, Solution-deposited and low temperature-annealed Eu^{3+}/Tb^{3+}-doped $CaMoO_4$/SrBaMoO4 luminescent thin films. J. Lumin. (2020). https://doi.org/10.1016/j.jlumin.2020.117371
13. W. Cai, T. Jiang, J. Fan, Coupling effects of thermal-humidity-sulfur aging on mechanical properties of (Ca, Sr)AlSiN3:Eu2+. Opt. Mater. (2022). https://doi.org/10.1016/j.optmat.2022.112384
14. ChanglinLiaoa, RenpingCaoa, WudiWanga, WenHua, GuotaiZhenga, ZhiyangLuob, PanLiu. Photoluminescence propertiesand energy transfer of $NaY(MoO_4)_2$:R(R=Sm^{3+}/Bi^{3+},Tb^{3+}/Bi^{3+},Sm^{3+}/Tb^{3+}) phosphors, Materials Research Bulletin. 97(2018).
15. Huan Duan, Ruirui Cui, Min Zhang, Chaoyong Deng. Photo luminescence properties and energy transfer studies of Ba_2YAlO_5:Sm^{3+}, Eu^{3+} orange-red phosphors, Journal for Light and Electron Optics. 238(2021) .
16. Q Zeng, W He, F Luan, D Guo.Luminescence and energy transfer of a novel $BaCeF_5$:Tb^{3+}, Eu^{3+}color-tunable phosphor, Colloids and Surfaces A Physicochemical and Engineering Aspects.(2022).
17. S. Wang, H. Zhang, T. Wang, S. Chunhui, H. Weihua, Preparation, fluorescence and energy transfer mechanism of Eu^{3+}-Sm^{3+} Co-doped glass ceramic containing $NaLa(MoO_4)_2$. J. Non-Crystalline Solids (2021). https://doi.org/10.1016/j.jnoncrysol.2021.120769
18. Du. Liang, Wu. Xiulan, Ou. Qiang Ren, Hai., Photoluminescence properties and energy transfer mechanism of new high-performance color-tunable LiLaSiO4:Tb3+, Eu3+ phosphors Polyhedron. Int. J. Inorg. Organomet. Chem. (2021). https://doi.org/10.1016/j.jnoncrysol.2021.120769
19. H Fan, Z Lu, Y Meng, P Chen, L Zhou, J Zhao, X He.Optical temperature sensor with superior sensitivity based on Ca_2LaSbO_6:Mn^{4+},Eu^{3+} phosphor, Optics & Laser Technology.148(2022).
20. M. Boshi, F. Zhao, Y. Chu, C. Li, J. Sun, Q. Zhao, S. Bai, Improvement of luminescence characteristics of $ZnGa_2O_4$:Tb^{3+} nanophosphors by Ce^{3+} codoping. Eur. J. Inorg. Chem.Inorg. Chem. (2022). https://doi.org/10.1002/ejic.202100976